Direct Visualization of Collective Wavepacket Dynamics

Richard M. Koehl, Satoru Adachi,† and Keith A. Nelson*

Department of Chemistry, Massachusetts Institute of Technology, Cambridge, Massachusetts 02139

Received: June 29, 1999; In Final Form: August 24, 1999

Direct spatiotemporal imaging of optic phonon−polariton wavepackets in polar crystals is demonstrated experimentally and described theoretically. Spatiotemporal imaging permits monitoring of wavepackets as they move through host samples at lightlike speeds. Different imaging methods may be used optimally for wavepackets with different spatial distributions, including spatially periodic or nonperiodic wavepackets. Spatiotemporal imaging holds particular promise for coherent phonon−polariton wavepacket control using spatiotemporal femtosecond pulse shaping.

I. Introduction

Quantum mechanical wavepacket excitation, manipulation, and observation are topics of considerable current interest.[1] In most cases, the wavepacket is a localized vibrational and/or electronic coherence composed of a superposition of molecular vibrational levels or Rydberg (or other) electronic states.[2−16] In these cases, localized excitation and detection fields are sufficient since wavepacket propagation does not involve motion of the excitation energy among different positions in the host medium. Complex optical excitation fields produced through femtosecond pulse shaping have been used for manipulation of many types of coherences,[1,11,13,15−23] and a wide variety of optical detection methods have been advanced. Visualization of molecular wavepacket dynamics through X-ray diffraction has also been proposed.[24]

In some cases, a collective polar lattice vibrational or electronic excitation may be coupled to an electromagnetic mode of similar frequency and wavevector. The resulting mixed excitation, called a polariton mode, propagates at lightlike speeds through the host. In the case of optic phonon−polaritons, coherent wavepacket propagation of the usual kind, in which neighboring ions undergo coherent vibrational oscillations with respect to each other, is accompanied by rapid motion of through the crystal. In this case, complete optical control and observation of wavepacket evolution require optical fields that extend over the entire range of polariton motion, which may substantially exceed the initial excitation region. For coherent optical control, a spatiotemporal femtosecond pulse shaping method has been developed which shows promise for automated generation of complex position and time-dependent optical waveforms, e.g. different femtosecond pulse sequences that can be directed to spatially separated regions of a crystal so that polaritons may be generated initially in one sample region and then manipulated in a specified manner as they propagate through the sample. The present paper deals with methods for *spatiotemporal polariton imaging*, through which real-space visualization of the complete spatial distribution of polaritonic excitations at various times may be carried out. The methods are demonstrated experimentally on optic phonon−polaritons in bulk lithium tantalate crystals, but should be applicable generally to bulk and surface or thin film polariton states of electronic or vibrational origin, and to polaritons in patterned or heterogenous media. Application to nonpropagating wavepackets is also possible, although in this case time-dependent spatial evolution is rarely a concern. A preliminary report of the imaging results has been presented.[25,26] Additional experimental results and description and a theoretical treatment are presented here.

Polariton propagation is a well-known phenomenon, and it has been observed in a wide variety of experiments. Optic phonon−polariton propagation has been monitored in time-resolved coherent anti-Stokes Raman scattering (CARS), inverse electrooptic Cerenkov shock-wave generation, and impulsive stimulated Raman scattering (ISRS) measurements through the use of a probe pulse whose time delay and spatial separation from the excitation pulse arrival time and position are varied proportionally.[27−38] These methods provide only partial information concerning spatial wavepacket evolution. For monitoring of the characteristic anisotropy of polaritonic responses, for elucidation of nonlinear lattice responses at large coherent phonon−polariton amplitudes, for observation of the polaritonic responses to complex excitation spatial and/or temporal profiles, or for feedback for and guidance of such excitation profiles with specified polariton wavepacket control objectives, visualization of the complete spatial as well as temporal evolution is essential. This is also important in cases of spatially heterogeneous samples, in which features such as ferroelectric domain morphologies, defects, concentration gradients in mixed crystals, and others may be characterized and their dielectric responses in the terahertz frequency range characterized. Facile visualization of spatiotemporal polariton wavepacket evolution is enabled by the methods demonstrated herein.

Phonon−polariton characterization is of general interest for elucidation of polar lattice dynamics and for study of structural phase transitions, in which the lowest-frequency phonon−polariton mode is often the "soft" mode whose collective motion mediates collective structural change.[39,40] In this sense, the soft mode plays the role of "collective reaction coordinate."[41−43] Time-resolved CARS and ISRS measurements and conventional Raman spectroscopy have been conducted with various scattering wavevectors (i.e., various scattering angles) to determine the phonon−polariton dispersion properties and at various sample temperatures to examine the characteristic reduction in soft mode vibrational frequencies (and corresponding divergence

† Permanent address: Department of Material Science, Himeji Institute of Technology, Hyogo 678-1297, Japan.

10.1021/jp9922007 CCC: $18.00
Published on Web 10/12/1999

in dielectric constants) associated with ferroelectric phase transitions.[29,31−38,44−46]

In the next section, a brief review of phonon−polariton properties and impulsive stimulated Raman scattering excitation and detection of phonon−polaritons is followed by a description and theoretical treatment of phonon−polariton imaging as conducted through various methods. An overview of the analysis and transformation of experimentally recorded polariton images into their spatial and temporal Fourier components is presented in section III. The general form of this analysis may be extended to many interesting cases, such as defect centers, dielectric−air boundaries, and arrays of dielectric media. The experimental measurements and their implications are discussed in section IV.

II. Generation and Detection of Propagating Phonon−Polaritons in Dielectric Media

A. Phonon−Polariton Properties. It is worthwhile to note that the phonon−polariton is the eigenmode of the system and an excitation in its own right, not merely a sum of both an electromagnetic field and a phonon.[47] The electromagnetic mode and the transverse polar optic phonon mode (ionic motions perpendicular to the wavevector **k**) have the same symmetry, so the wavevector-dependent crossing of the electromagnetic frequency (normally following the usual linear dispersion relation, $\omega/k = c/n$, with the refractive index $n(\omega)$ only weakly frequency-dependent) and the phonon frequency (normally essentially dispersionless with frequency ω_T = constant) is avoided. In the wavevector region around the avoided crossing, two mixed phonon−polariton modes which both have electromagnetic and polar vibrational character and which are both dispersive are formed. The phonon−polariton frequency range is typically about 1−10 THz.

Terahertz electromagnetic radiation propagating though a charge-free polar medium encounters a frequency-dependent dielectric function, due to the presence of the ions, which retards the progress of the radiation through the material. Maxwell's equations may be solved in combination with a description of the ionic contribution to the polarization and an equation of motion for the ions which includes (in the simplest case) a single vibrational resonance corresponding to a single optic phonon mode, leading to a macroscopic dielectric function[48−51]

$$\epsilon(\omega) = \epsilon_\infty + \frac{\omega_T^2(\epsilon_0 - \epsilon_\infty)}{\omega_T^2 - \omega^2 - i\omega\Gamma} \tag{2.1}$$

where ϵ_0 is the dielectric constant at frequencies well below the resonance, ϵ_∞ is the dielectric constant well above the resonance (but still potentially below other ionic and electronic resonances), ω_T is the frequency of the transverse optic phonon, and Γ is a phenomenological (frequency- and wavevector-independent) damping rate. The phonon−polariton dispersion is calculated by combining eq 2.1 with the expression $\epsilon^2(\omega) = n(\omega) = ck/\omega$.

When the crystal is anisotropic, the dielectric function becomes a tensor.[49] For uniaxial crystals with the polar mode parallel to the optic axis, as in lithium tantalate, the dielectric function tensor component of radiation polarized along the optic axis and propagating perpendicular to it (an extraordinary wave) is identical to the scalar dielectric function in eq 2.1.[49] The experiments described below correspond to this case. If propagation and polarization directions are both perpendicular to the optic axis and no other polar mode is present to couple to the radiation in that polarization (an ordinary wave), the dielectric function will be frequency independent but not necessarily equal to ϵ_∞, as contributions from electronic resonances might also differ along that polarization. For arbitrary propagation directions, the dielectric function will vary, and longitudinal and transverse polarizations may be mixed as well.[49]

Low-frequency phonon−polariton modes in ferroelectric materials give rise to large low-frequency dielectric constants ϵ_0 because the coupling between phonon and photon is large.[50] This is expressed by the Lyddane−Sachs−Teller relationship relating the limiting values of the dielectric retardance to the longitudinal and transverse optic phonon frequencies[48,50]

$$\epsilon_0/\epsilon_\infty = \omega_L^2/\omega_T^2 \tag{2.2}$$

where ω_L is the frequency of the longitudinal optic mode, which due to its symmetry does not couple to the electromagnetic radiation.[48] In the case of ferroelectric lithium tantalate ($LiTaO_3$) at room temperature, $\omega_T/2\pi c = 201$ cm^{-1} and $\omega_L/2\pi c = 402$ cm^{-1}.[46,52,53] Note that near ferroelectric phase transitions, the softening of the transverse phonon frequency ω_T is associated with the divergence of the low-frequency dielectric constant ϵ_0.

Many techniques have been used to study phonon−polaritons in dielectric media. Several ultrafast techniques, based on the inverse electrooptic effect, difference frequency mixing, and impulsive stimulated Raman scattering, have been applied to the study of these excitations.[27−37] In the experiments described here, ultrashort optical pulses excite a polar phonon−polariton mode primarily through nonresonant impulsive stimulated Raman scattering (ISRS).[31,51,54−56] When the optical pulse duration is much shorter than the oscillation period of the (Raman-active) mode, stimulated Raman scattering occurs through mixing among the frequency components contained within the broad optical bandwidth. This exerts an "impulse" driving force that excites the coherent phonon−polariton wavepacket. The coherent phonon−polariton response results in a modulation of the sample's optical refractive index which moves as the response propagates through the medium. For example, if the optical excitation field consists of a pair of pulses spatially and temporally overlapped to form an interference "grating" pattern with a well-defined wavevector, then the refractive index modulation matches this pattern from which probe light may be coherently scattered (i.e., "diffracted"). If the optical excitation field consists of a single tightly focused pulse, the spatially localized polariton response contains a wide range of wavevector magnitudes and orientations, and an anisotropic "ripple"-like response occurs with a corresponding time and position-dependent modulation of the refractive index. In previous observations of phonon−polariton propagation, spatially and temporally delayed probe pulses were used to monitor such propagating responses through measurement of coherent scattering or depolarization. In diffraction measurements, the ISRS signal is proportional to the square of the dielectric response function,[51,54−56]

$$I(\mathbf{r},t) \propto |G_{\epsilon\epsilon}(\mathbf{r},t)|^2 \tag{2.3}$$

In some cases, the diffracted field is mixed with either scattered probe light or an undiffracted reference pulse to create a heterodyne signal and retrieve the phase of the spatial and temporal dielectric response function $G_{\epsilon\epsilon}(\mathbf{r},t)$.[34,35,57−59] In depolarization measurements with tightly focused excitation and probe pulses, the signal also reflects the phase of the response function.

B. Spatiotemporal Polariton Imaging. The novel feature of the experiment at hand is that the temporally delayed probing

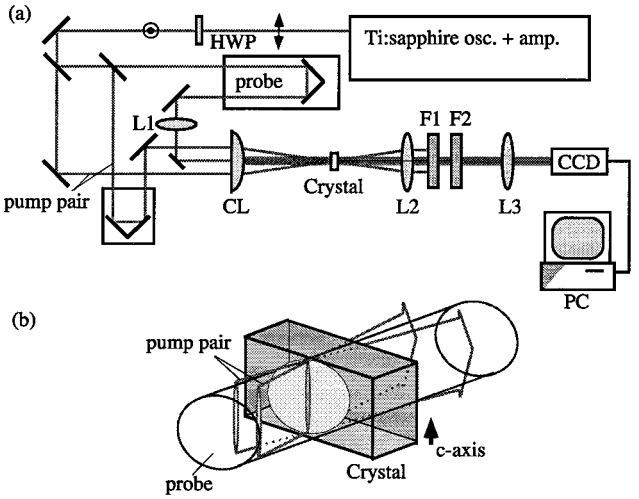

Figure 1. (a) Experimental apparatus. A 40 fs, 800 nm laser pulse is split into two 20 μJ pump pulses and one 60 μJ probe pulse. The pump pulses are focused by a cylindrical lens CL onto the crystal, where they cross to form a grating pattern. (In some cases, only one pump pulse is used.) A spherical lens L1 before the cylindrical lens defocuses the probe pulse, which is incident onto a large region of the crystal. The pump and probe pulses copropagate through the crystal. A telescope (lenses L2 and L3) images the wide probe spot onto a CCD. Filters F1 and F2 within the telescope remove second harmonic and fundamental pump light, and a PC digitizes and stores the data for later processing. (b) Typical geometry of pump and probe pulses at sample. All pulses are polarized parallel to the optic axis (*c*-axis) shown here. A pair of pump pulses is focused by CL to form a grating at the sample. The wide probe pulse copropagates with the pump pulses through the sample. Other geometries, such as a single pump pulse focused to a line or a round spot, are also possible.

pulse is not diffracted into a single selected order from the excitation region but is instead imaged in transmission, permitting the visualization of the moving phonon−polariton wavepacket in both space and time. The temporally delayed probing pulse spot size is significantly larger than the excitation region, and imaging in transmission allows the traveling phonon−polariton wavepacket to be viewed as it moves through the sample. The spatial variation of the dielectric phase modulation at a particular time delay is encoded into the spatial phase profile of the transmitted probe pulse. Conversion of this spatial phase modulation into an amplitude modulation is achieved using either the Talbot self-imaging phenomenon or phase-contrast microscopy as described further below. In either case the amplitude modulation is imaged onto a camera or CCD detector as shown in Figure 1. The conversion of a phase object (the phonon−polariton refractive index modulation) into an amplitude image by self-imaging or by filtering spatial Fourier components of the probe is a type of heterodyne technique in which the local oscillator is taken as one spatial Fourier component, often the zero-order transmitted light, which beats against the signal in other spatial Fourier components. As a heterodyne measurement, this gives information about both the phase and amplitude of the spatial and temporal response function $G(\mathbf{r},t)$.

The Talbot self-imaging phenomenon needed for the present experiments has been studied extensively since its discovery in 1836.[60] Patorski has reviewed the self-imaging effect in detail, considering combinations of coherent, partially coherent, and incoherent illumination, objects consisting of combinations of phase and amplitude gratings, and illumination by plane waves and Gaussian beams.[61] If an object has a well-defined spatial period, as is found in a grating, Fresnel diffraction forms nearly identical copies of the original object in a sequence of planes immediately after it. There are also separate planes between these autoreplication planes where amplitude modulations are converted into phase modulations and vice versa. The distance from the object to each autoreplication or phase-to-amplitude plane depends on the size of the primary spatial frequency component of the object.

What follows is a simple quantitative explanation of the Talbot effect in terms of Fresnel diffraction of plane waves near a coherently illuminated planar object. Consider an electric field amplitude u_0 immediately after a phase object at $z = 0$, so that

$$u_0(x,y) = \exp(i\alpha \cos(k_{x0}x)) \tag{2.4}$$

and the magnitude of the spatial phase variation α is assumed to be small enough that

$$u_0(x,y) \approx 1 + i\alpha \cos(k_{x0}x) \tag{2.5}$$

The period of the sinusoidal spatial phase variation is $d = 2\pi/k_{x0}$. Note that

$$|u_0(x,y)|^2 = 1 + \text{second-order terms} \approx 1 \tag{2.6}$$

The spatial Fourier transform[62]

$$U_0(k_x,k_y) = \frac{1}{(2\pi)^2}\int_{-\infty}^{\infty}\int_{-\infty}^{\infty} u_0(x,y)\exp(-ik_x x - ik_y y)\,dx\,dy \tag{2.7}$$

of the phase object is in this case

$$U_0(k_x,k_y) = \left(\delta(k_x) + i\frac{\alpha}{2}\delta(k_x - k_{x0}) + i\frac{\alpha}{2}\delta(k_x + k_{x0})\right)\delta(k_{y0}) \tag{2.8}$$

It is assumed that coherent light of central wavelength $\lambda = 2\pi/k$ is incident on the phase object. Fresnel diffraction at a distance z from an object is described in real space in the paraxial limit as a convolution

$$u(x,y,z) = \frac{1}{i\lambda z}\int_{-\infty}^{\infty} dx_0 \int_{-\infty}^{\infty} dy_0\, u_0(x_0,y_0)\exp\left(i\frac{k}{2z}[(x - x_0)^2 + (y - y_0)^2]\right) \tag{2.9}$$

or equivalently in Fourier space by a multiplication[62]

$$U(k_x,k_y,z) = (2\pi)^2 H(k_x,k_y,z)U_0(k_x,k_y) \tag{2.10}$$

where the Fresnel kernel is

$$H(k_x,k_y,z) = \left(\frac{1}{2\pi}\right)^2 \exp(-i[k_x^2 + k_y^2]z/2k) \tag{2.11}$$

When the distance $z = d^2/2\lambda = \pi k/k_{x0}^2$, then

$$H\left(k_x,k_y,z = \frac{d^2}{2\lambda}\right) = \left(\frac{1}{2\pi}\right)^2 (-i)^{(k_x^2/k_{x0}^2)} \exp(-i\pi k_y^2/2k_{x0}^2) \tag{2.12}$$

so that

$$U\left(k_x,k_y,z = \frac{d^2}{2\lambda}\right) = \left(\delta(k_x) - \frac{\alpha}{2}\delta(k_x - k_{x0}) - \frac{\alpha}{2}\delta(k_x + k_{x0})\right)\delta(k_y)\exp(-i\pi k_y^2/2k_{x0}^2) \tag{2.13}$$

as can be seen by performing the inverse Fourier and Fourier

transforms in succession. The real-space field is

$$u\left(x,y,z=\frac{d^2}{2\lambda}\right)=1-\alpha\cos(k_{x0}x) \tag{2.14}$$

and to first order the real-space intensity is

$$|u\left(x,y,z=\frac{d^2}{2\lambda}\right)|^2=1-2\alpha\cos(k_{x0}x) \tag{2.15}$$

At this and other odd integral multiples of $z=d^2/2\lambda=\pi k/k_{x0}^2$, the phase grating is converted into an amplitude grating by the transfer function of eq 2.12. The image contains a $(2n+1)\lambda/2$ phase shift of the $\pm k_{x0}$ spatial components relative to the zero-order spatial component. At even integral multiples of $z=d^2/2\lambda=\pi k/k_{x0}^2$, the $n\lambda$ phase shift of the $\pm k_{x0}$ spatial components replicates the phase grating as another phase grating. The zero-order spatial component acts as a local oscillator to the $\pm k_{x0}$ spatial components so that the signal, as in other measurements that utilize optical heterodyne detection, is proportional to the phase modulation

$$I(\mathbf{r},t)\propto G_{\epsilon\epsilon}(\mathbf{r},t) \tag{2.16}$$

rather than its square. Far away from the object, the paraxial limit and this analysis break down.

For a phase grating given by eq 2.5 with arbitrarily large phase modulation α, Patorski gives the corresponding amplitude grating image at an odd multiple of $d^2/2\lambda$ as

$$|u\left(x,y,z=(2n+1)\frac{d^2}{2\lambda}\right)|^2=1+(-1)^n\sin(2\alpha\cos(k_{x0}x))=$$
$$1+2(-1)^n\sum_{l=1}^{\infty}(-1)^{l-1}J_{2l-1}(2\alpha)\cos([2l-1]k_{x0}x) \tag{2.17}$$

Only odd spatial harmonics contribute to the amplitude grating at the image plane. The lowest-order nonlinear lattice effect in this polar medium, second harmonic generation, should produce even spatial harmonics, which could easily be differentiated from these optical harmonic effects in the signal.

The application of the Talbot effect to femtosecond time-resolved spectroscopy is straightforward. In Figure 1, a two-lens telescope images the sample onto a CCD. The telescope reproduces the object plane at the image plane. In the vicinity of the image plane of the two-lens telescope, the Talbot effect converts the phase modulation into amplitude modulation as described above. The CCD displacement along the z (propagation) axis is adjusted to maximize the phase to amplitude conversion at the detector.

Many related phase-imaging techniques will give phase to amplitude conversion. In phase contrast microscopy,[63,64] a glass slide or other delay advances or retards the phase of the zeroth-order spatial frequency component relative to all the other spatial frequency components in order to achieve phase to amplitude conversion of an object at the image plane. (Note that as described above, if no operation is performed on any of the transmitted spatial components, the phase object is simply reproduced in the image plane as a phase image, not an amplitude image.) With ultrashort pulses, the zeroth-order spatial component must not be advanced or retarded more than a few optical cycles relative to the other spatial components, or else temporal overlap and heterodyne mixing among the components will be lost. It is also possible to convert phase information into amplitude information by blocking selected spatial frequency components. For example, a detector may be placed in the image plane of a two-lens telescope and all the spatial frequency components to one side of the zeroth-order component may be blocked after the first lens in the telescope, e.g. we block all $k_x<0$, so that the image at the detector is a sum of the spatial frequency components with $k_x\geq 0$. For the phase-modulated object in eq 2.5, the Fourier-space field at the image in this case is

$$U(k_x,k_y,z=0)=\left(\delta(k_x)+i\frac{\alpha}{2}\delta(k_x-k_{x0})\right)\delta(k_{y0}) \tag{2.18}$$

In real space, the field at the image is

$$u(x,y,z=0)=1+i\frac{\alpha}{2}\exp(ik_{x0}x) \tag{2.19}$$

and to lowest order in α the image intensity is

$$|u(x,y,z)|^2=1-\alpha\sin(k_{x0}x) \tag{2.20}$$

Again there is a linear phase to amplitude conversion, but in this case the conversion does not depend on k_{x0} or z. Thus it is possible to form images of more arbitrary spatial phase patterns that do not have a well-defined spatial periodicity. For a spatial phase object represented as a Fourier sum

$$u_0(x,y)=1+i\sum_n(\alpha_n\cos(k_{xn}x)+\beta_n\sin(k_{xn}x)) \tag{2.21}$$

the image intensity to lowest order is

$$|u(x,y,z)|^2=1+\sum_n(-\alpha_n\sin(k_{xn}x)+\beta_n\cos(k_{xn}x)) \tag{2.22}$$

The modulation in the image intensity is proportional to the spatial derivative of the modulation of the phase. This Schlieren technique is well-known.[62,63]

III. Experimental Results

We have performed spatiotemporal imaging experiments using ferroelectric lithium tantalate ($LiTaO_3$), which possesses a polar optic phonon mode associated with its ferroelectric−paraelectric structural phase transition. The properties of the mixed phonon−polariton mode created by the coupling of this strongly polar lattice mode with far-infrared radiation are well-known.[48,49,51] The frequency of the uncoupled lattice resonance is $\omega/2\pi c=201\ \mathrm{cm}^{-1}$, and the low-frequency dielectric constant ϵ_0 is 38.4. The frequency of the corresponding longitudinal optic phonon oscillation is 402 cm^{-1}, and the effective high-frequency dielectric constant ϵ_∞ is 9.6. In order to impulsively drive and observe the response, the pump and probe beams should have a temporal duration shorter than the vibrational oscillation period, which is as short as 165 fs in the lower polariton branch of $LiTaO_3$.[46,54]

Both 1 mm × 4 mm × 2 mm and 2 mm × 4 mm × 2 mm ($X\times Y\times Z$) X-cut crystals have been used. The polar (Z) axis is aligned with the polarization of the pump and probe beams. Two lenses after the crystal form a microscope that is used to image the transmitted probe light onto a CCD. A slight downward tilt of the probe beam at the crystal before the first

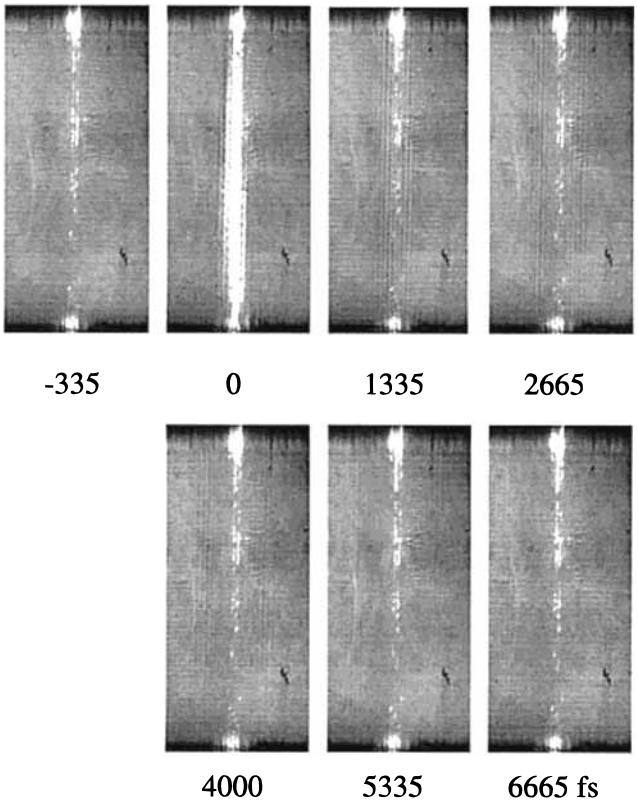

Figure 2. Images of propagating phonon polaritons produced by impulsive grating excitation with wavevector $q \approx 2100\ \mathrm{cm}^{-1}$. Although only seven frames are shown, 221 frames were recorded at 35 fs intervals. Image dimensions 2050 μm tall × 895 μm wide.

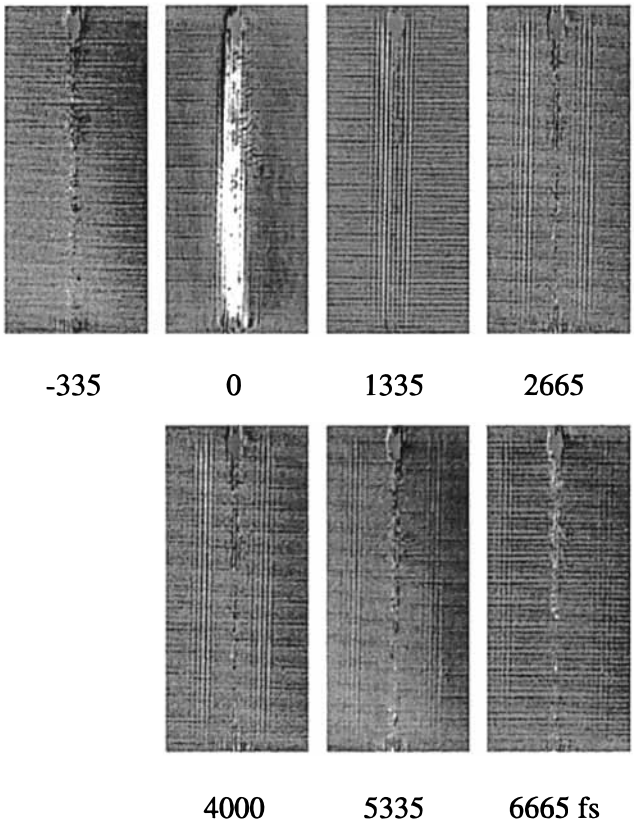

Figure 3. To improve the quality of the images in Figure 2 for quantitative analysis, 11 scans taken well before time $t = 0$ were averaged and subtracted from the raw data. Image dimensions 2050 μm tall × 895 μm wide.

lens leads to a vertical separation between excitation and probe beams after the first lens. The excitation pulses are removed with a specially shaped BG-39 filter that does not block the probing pulse. A subsequent RG-780 long-pass filter removes second-harmonic optical signals, and a series of neutral-density filters equivalent to OD 4-7 lower the probe pulse intensity. The wavevector of the grating for a given laser setup can be calculated according to ref 46. Measurements made with this method agree with observations of the grating wavevector at the CCD, where the image pixel size is calibrated with a target pattern of known size in the sample plane. The CCD integrates the incident light until it is read at the NTSC frame rate of about 30 frames/s. An 8-bit PC-compatible frame grabber (DigitalVision RT Mono) digitizes the signal, and the PC stores it for later processing.

Representative data for a typical Talbot-effect experiment are shown in Figure 2. The complete data set for that particular experiment consists of 221 images. 10 of these images from the delay region before $t = 0$ are averaged and subtracted from the remaining 211 images to eliminate background noise (Figure 3). This background subtraction step is not needed to view the data, but it does reduce noise from scattered light. The image files also may be collated to form a moving picture of the far-infrared light wave as it propagates through the crystal.

The record of CCD images shows the signal as a function of two spatial dimensions and one temporal dimension. It is possible, for excitation and propagation characteristics that only depend on one spatial dimension, to reduce this vast quantity of information to just one spatial and one temporal dimension and improve the signal to noise ratio by averaging over the vertical columns. The sequence of 211 background-subtracted images may be collated into a single signal $I(r_x,t)$ by averaging the signal in the vertical direction in each image and displaying the real-space average at each real-time data point. Figure 4 displays this condensation for the data in Figures 2 and 3, but at all 211 time data points.

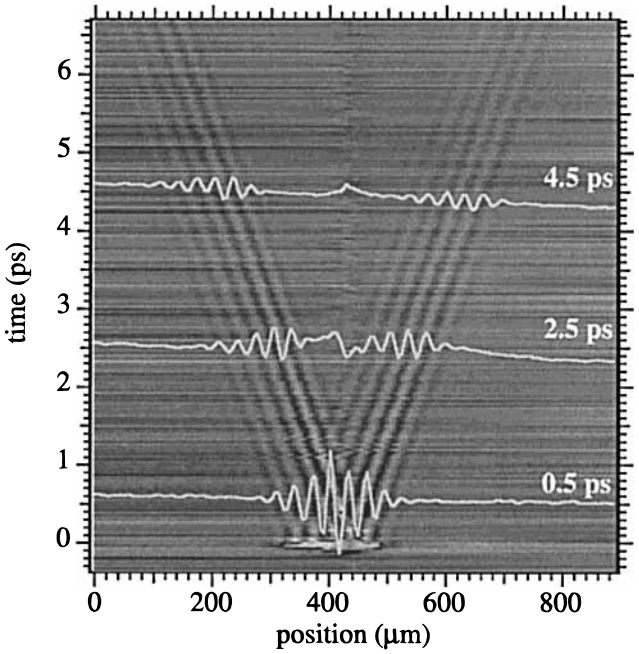

Figure 4. Condensation of the entire data set sampled in Figures 2 and 3. The space- and position-dependent signal $I(r_x,t)$ is put into this form by averaging the signal in the vertical (y) direction in each image and displaying the real-space average at each real-time data point. Data at 0.5, 2.5, and 4.5 ps are overlaid for reference.

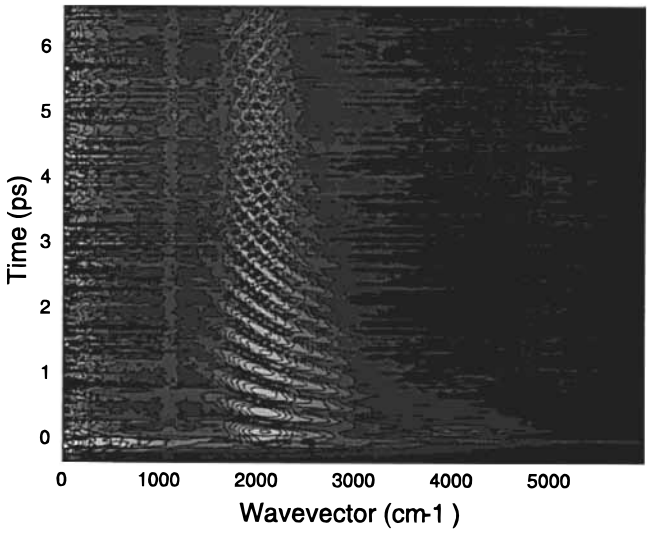

Figure 5. **n**(**q**,*t*) for the image data shown in Figure 3. Application of the discrete Fourier transform (DFT) to the image data shown in Figure 3 shows the spatial and temporal evolution of the polariton wavepacket. The contour axis is logarithmic and is calculated with arbitrary units.

The spatiotemporal images, which record the positions and spatial profiles in real space of the wavepacket at particular times, also may be transformed into their Fourier components in both time and space. A transformation along the one remaining spatial axis in Figure 4 allows the relationships between the wavevector components in the coherent-state wavepacket to be studied as functions of time. The signal after the DFT is

$$I(k_x,t) = I_0(k_x)\, e^{-\gamma t} \sin(\omega t + \varphi) \qquad (3.1)$$

Because the DFT is complex, we plot only the amplitude of eq 3.1 in Figure 5. This plot of signal as a function of wavevector and time yields an extraordinarily large amount of information about propagating phonon−polaritons. The real-space wavepacket at any point in time has been transformed into its wavevector components. The apparent real-space damping of the moving packet of fringes (Figures 2−4) is due in large part to the different phase velocities of the packet's wavevector components, which cause the components to spread out of phase over time.

By plotting the amplitude of a particular polariton wavevector component as a function of time, we may measure the frequency and damping rate of the selected component and compare this result with previous values obtained by other space- and time-dependent ultrafast techniques or by angle-dependent Raman spectroscopy. The data analysis is more tractable if the fit is to the square of the DFT

$$|I(k_x,t)|^2 = {}^1/_2|I_0(k_x)|^2\, e^{-2\gamma t}\,(1 - \cos(2\omega t + 2\varphi)) \quad (3.2)$$

A fit between this model and the signal is shown in Figure 6 for the 1760 cm^{-1} line in Figure 5. Because the entire wavepacket is on the CCD camera at all times, the signal is not modulated with the Gaussian envelope seen in previous spatiotemporal grating experiments.[33−35] The fit has parameters $\gamma = 1.13$ cm^{-1} and $\omega = 47.0$ cm^{-1}, corresponding to a refractive index $n(\omega) = ck/\omega = 37.4$. The observed damping rate of the polariton is wavevector-dependent (in contrast with the phenomenological wavevector-independent damping of eq 2.1) because the degree of phonon character changes with wavevector and because, as the frequency varies, other lattice phonon modes

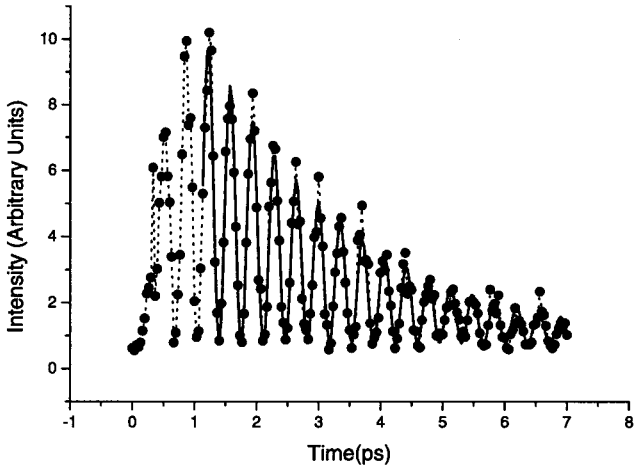

Figure 6. Fit (solid line) between eq 3.2 and the 1760 cm^{-1} signal (circles) of Figure 4. Fit parameters $\gamma = 1.1$ cm^{-1} and $\omega = 47.0$ cm^{-1}

.

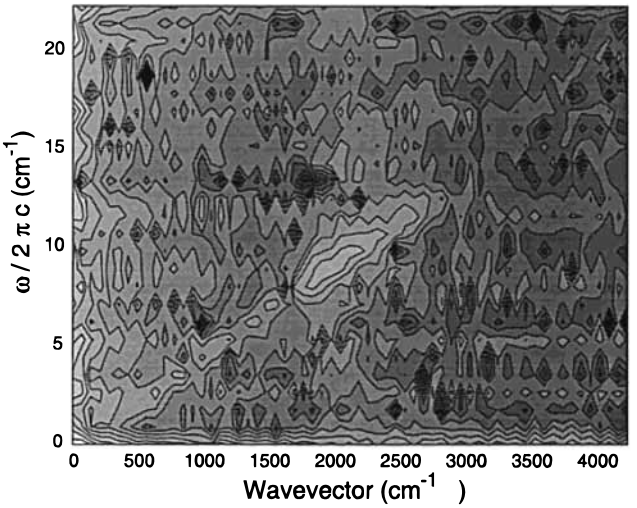

Figure 7. **n**(**q**,ω) for the image data shown in Figure 3. Two applications of the DFT to the image data shown in Figure 3 (compare Figure 4) show the spatial and temporal evolution of the polariton wavepacket. The grayscale axis is logarithmic and is calculated with arbitrary units.

with which the polar mode is coupled may come into resonance. At higher wavevectors, it is necessary to introduce additional phonon resonances to fit the observed wavevector-dependent damping.[46] Previous ultrafast studies of $LiTaO_3$ at room temperature have observed damping rates of 1.8 cm^{-1} using position-independent ISRS at 1700 cm^{-1},[46] 0.67 cm^{-1} using position-dependent heterodyne detection with parasitically scattered probe light at 900 cm^{-1}.[35]

Finally, it is possible to convert the signal as a function of wavevector and time $I(k_x,t)$ into a plot of the signal as a function of wavevector and frequency $I(k_x,\omega)$ by applying the DFT along the time axis to each complex wavevector component calculated using eq 3.1. The signal density is localized on the dispersion curve (Figure 7). The signal is seen only on the lower branch of the dispersion curve at $\omega(k)$ and not on the upper branch. Points near $t = 0$, where electronic effects and diffracted light coupled from the pump beams distort the spatial profile of the response, have been excluded.

At the comparatively low excitation intensities used in this experiment, neither wavevector harmonics nor frequency harmonics of the fundamental excited wavepacket were clearly observed in the signal.[65,66]

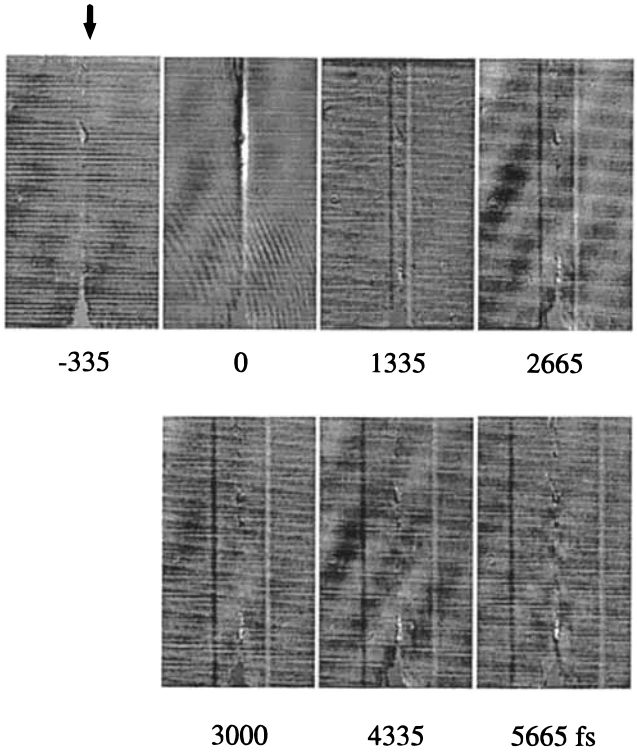

Figure 8. Samples of image data from propagating phonon polaritons produced by a single excitation beam focused to a line and imaged by the Schlieren method. Background data have been subtracted as in Figure 3.

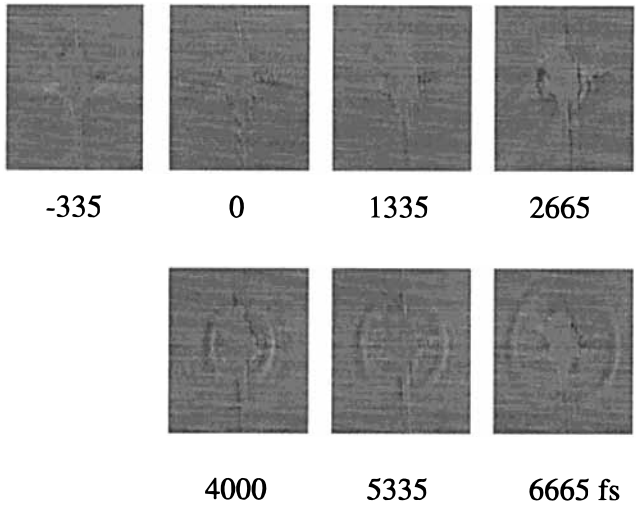

Figure 9. Images from propagating phonon polaritons produced by a single beam focused to a round spot. Background data have been subtracted as in Figure 3. The splotch in the center that obscures some data near time $t = 0$ is due to intense scattered pump light, which could not be completely filtered from the imaging setup. Image dimensions 1020 μm tall $\times$ 860 μm wide.

Figure 8 shows selected images from a data set taken with a single cylindrically focused excitation pulse polarized parallel to the optic axis. Phase-to-amplitude conversion was accomplished by blocking all orders of diffraction to one side of the zeroth-order beam. The initial polarization induced by the optical pulse radiates outward in a wedge shape.[30,67] The image of the distribution of the far-infrared transient pulse is its spatial derivative, which creates an apparent asymmetry between the left and right hand sides of the shock wedge.[30,67]

As the polarization of radiation changes from an extraordinary wave at $\theta = 0$ with the polar resonance to an ordinary wave at

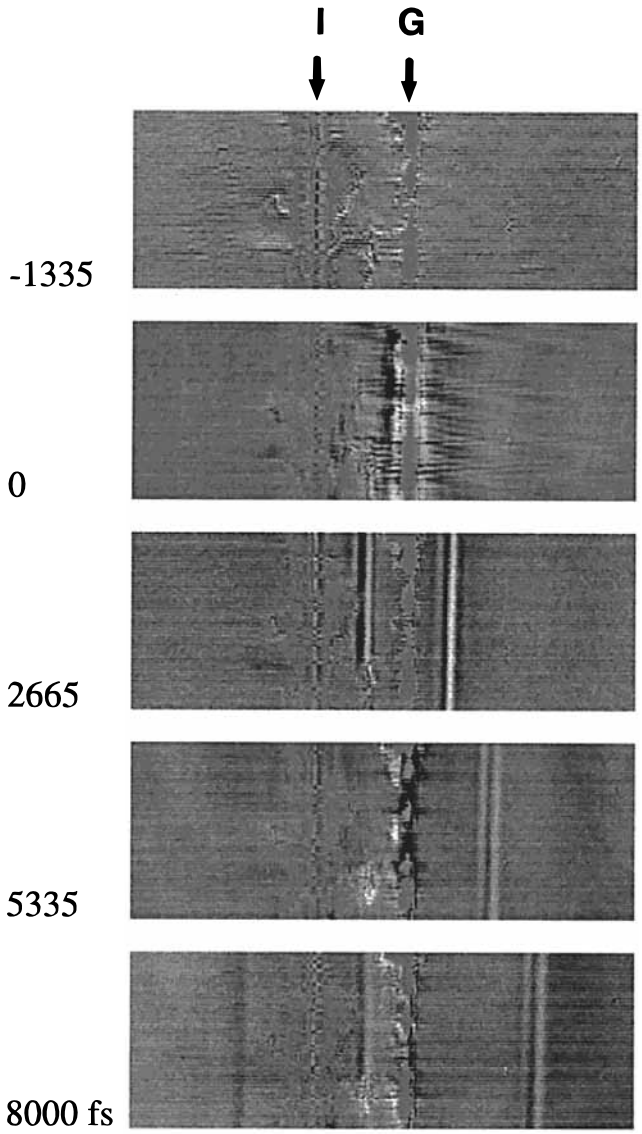

Figure 10. Samples of image data from propagating phonon polaritons generated at line G by a single focused excitation beam. The phonon polaritons are partially transmitted through and partially reflected by a crystal−air−crystal interface I. Background data have been subtracted as in Figure 3. The crystal surfaces through which the polaritons pass are ground but not polished. Apparent defects near the interface are actually chips at the corners of the crystals that deflect optical probe light but do not interfere with polariton propagation.

$\theta = \pi/2$ without the resonance, the dielectric function in a uniaxial crystal has the form[63]

$$\frac{1}{\epsilon(\omega,\theta)} = \frac{\sin^2\theta}{\epsilon_0} + \frac{\cos^2\theta}{\epsilon_e(\omega)} \tag{3.3}$$

Figure 9 shows selected images from a data set taken with a single tightly focused excitation pulse which is polarized parallel to the optic axis. Phase-to-amplitude conversion was achieved again by blocking all orders of diffraction to one side of the zeroth-order beam. The initial polarization induced by the optical pulse is also polarized parallel to the optic axis, but any region of the radiated shock cone is polarized perpendicular to the direction of its outward propagation.[30,67] As the shock cone radiates outward, two effects are seen. Because any region of the shock cone is polarized perpendicular to the direction of propagation, the efficiency of diffraction diminishes as coupling to the polar mode falls away in the vertical direction in the

figure. Also, the phase velocity of the shock cone rises as the dielectric constant diminishes. Interpretation of these effects is complicated by the spatial derivative inherent in this method. However, note that no images are seen when the excitation pulses are polarized perpendicular to the optic axis, nor are they seen when blocking all orders of diffraction above or below the zeroth-order beam.

Besides the polariton generation experiments of the type shown above, reflection and propagation across interfaces[37] have also been seen, as shown in Figure 10.

IV. Conclusions

A method for the measurement in dielectric media of the far-infrared space- and time-dependent response $\chi(\mathbf{r},t)$ to an impulsive optical driving force through phase-to-amplitude conversion of a probing optical pulse has been demonstrated. The ability to visualize propagating phonon−polaritons moving through anisotropic media, defects, and interfaces will be of substantial utility in characterization of long-term or transient heterogeneities due to domain reversals, optical or electrical signals, or other causes and in future attempts to measure and manipulate excitations with higher phonon−polariton intensities. Manipulation of propagating phonon−polaritons, which may be suitable as high-bandwidth coherent signal carriers in optimized hosts, with spatiotemporally shaped optical fields will be greatly facilitated with the monitoring capabilities demonstrated.

Acknowledgment. This work was supported in part by NSF Grant No. CHE-9713388. We appreciate stimulating discussions with T. F. Crimmins and G. P. Wakeham.

References and Notes

(1) Kohler, B.; Krause, J. L.; Raksi, F.; Wilson, K. R.; Yakovlev, V. V.; Whitnell, R. M.; Yan, Y. *Acc. Chem. Res.* **1995**, *28*, 133.

(2) Dantus, M.; Rosker, M. J.; Zewail, A. H. *J. Chem. Phys.* **1987**, *87*, 2395.

(3) ten Wolde, A.; Noordam, L. D.; Lagendijk, A.; van Linden van den Heuvell, H. B. *Phys. Rev. Lett.* **1988**, *61*, 2099.

(4) Yeazell, J. A.; Mallalieu, M.; Parker, J.; C.R. Stroud, J. *Phys. Phys. Rev. A* **1989**, *40*, 5040.

(5) Scherer, N. F.; Carlson, R. J.; Matro, A.; Du, M.; Ruggiero, A. J.; Romero-Rochin, V.; Cina, J. A.; Fleming, G. R.; Rice, S. A. *J. Chem. Phys.* **1991**, *95*, 1487.

(6) Scherer, N. F.; Matro, A.; Du, M.; Carlson, R. J.; Cina, J. A.; Fleming, G. R. *J. Chem. Phys.* **1992**, *96*, 4180.

(7) Planken, P. C. M.; Nuss, M. C.; Brener, I.; Goossen, K. W.; Luo, M. S. C.; Chuang, L.; Pfeiffer, L. *Phys. Rev. Lett.* **1992**, *69*, 3800.

(8) Krause, J. L.; Whitnell, R. M.; Wilson, K. R.; Yan, Y.; Mukamel, S. *J. Chem. Phys.* **1993**, *99*, 6562.

(9) Planken, P. C. M.; Brener, I.; Nuss, M. C.; Luo, M. S. C.; Chuang, S. L. *Phys. Rev. B* **1993**, *48*, 4903.

(10) Bardeen, C. J.; Wang, Q.; Shank, C. V. *Phys. Rev. Lett.* **1995**, *75*, 3410.

(11) Kohler, B.; Yakovlev, V. V.; Che, J.; Krause, J. L.; Messina, M.; Wilson, K. R.; Schwenter, N.; Whitnell, R. M.; Yan, Y. *Phys. Rev. Lett.* **1995**, *74*, 3360.

(12) Schumacher, D. W.; Hoogenraad, J. H.; Pinkos, D.; Bucksbaum, P. H. *Phys. Rev. A* **1995**, *52*, 4719.

(13) Bardeen, C. J.; Che, J.; Wilson, K. R.; Yakovlev, V. V.; Apkarian, V. A.; Martens, C. C.; Zadoyan, R.; Kohler, B.; Messina, M. *J. Chem. Phys.* **1997**, *106*, 8486.

(14) Cao, J.; Wilson, K. R. *J. Chem. Phys.* **1997**, *107*, 1441.

(15) Weinacht, T. C.; Ahn, J.; Bucksbaum, P. H. *Phys. Rev. Lett.* **1998**, *80*, 5508.

(16) Weinacht, T. C.; Ahn, J.; Bucksbaum, P. H. *Nature* **1999**, *397*, 233.

(17) Weiner, A. M.; Leaird, D. E.; Wiederrecht, G. P.; Nelson, K. A. *Science* **1990**, *247*, 1317.

(18) Brener, I.; Planken, P. C. M.; Nuss, M. C.; Pfeiffer, L.; Leaird, D. E.; Weiner, A. M. *Appl. Phys. Lett.* **1993**, *63*, 2213.

(19) Brener, I.; Planken, P. C. M.; Nuss, M. C.; Luo, M. S. C.; Chuang, S. L.; Pfeiffer, L.; Leaird, D. E.; Weiner, A. M. *J. Opt. Soc. Am. B* **1994**, *11*, 2457.

(20) Wefers, M. M.; Kawashima, H.; Nelson, K. A. *J. Chem. Phys.* **1995**, *102*, 9133.

(21) Bardeen, C. J.; Yakovlev, V. V.; Wilson, K. R.; Carpenter, S. D.; Weber, P. M.; Warren, W. S. *Chem. Phys. Lett.* **1997**, *280*, 151.

(22) Bardeen, C. J.; Che, J.; Wilson, K. R.; Yakovlev, V. V.; Cong, P.; Kohler, B.; Krause, J. L.; Messina, M. *J. Phys. Chem. A* **1997**, *101*, 3815.

(23) Wefers, M. M.; Kawashima, H.; Nelson, K. A. *J. Chem. Phys.* **1998**, *108*, 10248.

(24) Cao, J. S.; Wilson, K. R. *J. Phys. Chem. A* **1999**, *102*, 9523.

(25) Koehl, R. M.; Adachi, S.; Nelson, K. A. *J. Chem. Phys.* **1999**, *110*, 1317.

(26) Adachi, S.; Koehl, R. M.; Nelson, K. A. *Butsuri* **1999**, *54*, 357.

(27) Auston, D. H.; Cheung, K. P.; Valdmanis, J. A.; Kleinman, D. A. *Phys. Rev. Lett.* **1984**, *53*, 1555.

(28) Cheung, K. P.; Auston, D. H. *Phys. Rev. Lett.* **1985**, *55*, 2152.

(29) Gale, G. M.; Vallée, F.; Flytzanis, C. *Phys. Rev. Lett.* **1986**, *57*, 1867.

(30) Auston, D. H.; Nuss, M. C. *IEEE J. Quant. Electron.* **1988**, *QE-24*, 184.

(31) Etchepare, J.; Grillon, G.; Antonetti, A.; Loulergue, J. C.; Fontana, M. D.; Kugel, G. E. *Phys. Rev. B* **1990**, *41*, 12362.

(32) Vallée, F.; Flytzanis, C. *Phys. Rev. B* **1992**, *46*, 13799.

(33) Planken, P. C. M.; Noordam, L. D.; Kennis, J. T. M.; Lagendijk, A. *Phys. Rev. B* **1992**, *45*, 7106.

(34) Bakker, H. J.; Hunsche, S.; Kurz, H. *Phys. Rev. Lett.* **1992**, *69*, 2823.

(35) Bakker, H. J.; Hunsche, S.; Kurz, H. *Phys. Rev. B* **1993**, *48*, 13524.

(36) Bakker, H. J.; Hunsche, S.; Kurz, H. *Phys. Rev. B* **1994**, *50*, 914.

(37) Vallée, F.; Flytzanis, C. *Phys. Rev. Lett.* **1995**, *74*, 3281.

(38) Qiu, T.; Maier, M. *Phys. Rev. B* **1997**, *56*, R5717.

(39) Lines, M. E.; Glass, A. M. *Principles and Applications of Ferroelectrics and Related Materials*; Clarendon Press: Oxford, UK, 1977.

(40) Bruce, R. D.; Cowley, R. A. *Structural Phase Transitions*; Taylor & Francis: London, 1981.

(41) Dougherty, T. P.; Wiederrecht, G. P.; Nelson, K. A.; Garrett, M. H.; Jensen, H. P.; Warde, C. *Science* **1992**, *258*, 770.

(42) Fahy, S.; Merlin, R. *Phys. Rev. Lett.* **1994**, *73*, 1122.

(43) Nelson, K. A. Coherent control of optics, molecules, and materials. In *Ultrafast Phenomena IX*; Mourou, G. A., Zewail, A. H., Barbara, P. F., Knox, W. H., Eds.; Springer-Verlag: Springer-Verlag:Berlin, 1994.

(44) Kien, D. P.; Loulergue, J. C.; Etchepare, J. *Phys. Rev. B* **1993**, *47*, 11027.

(45) Loulergue, J. C.; Etchepare, J. *Phys. Rev. B* **1995**, *52*, 15160.

(46) Wiederrecht, G. P.; Dougherty, T. P.; Dhar, L.; Nelson, K. A.; Leaird, D. E.; Weiner, A. M. *Phys. Rev. B* **1995**, *51*, 916.

(47) Artoni, M.; Birman, J. L. *Phys. Rev. B* **1991**, *44*, 3736.

(48) Born, M.; Huang, K. *Dynamical Theory of Crystal Lattices*; Clarendon Press: Oxford, UK, 1954.

(49) Barker, A. S.; Loudon, R. *Rev. Mod. Phys.* **1972**, *44*, 18.

(50) Mills, D. L.; Burstein, E. *Rep. Prog. Phys.* **1974**, *37*, 817.

(51) Dougherty, T. P.; Wiederrecht, G. P.; Nelson, K. A. *J. Opt. Soc. Am. B* **1992**, *9*, 2179.

(52) W. D. Johnston, J.; Kaminow, I. P. *Phys. Rev.* **1968**, *168*, 1045.

(53) Kaminow, I. P.; W. D. Johnston, J. *Phys. Rev.* **1967**, *160*, 519.

(54) Yan, Y.-X.; Gamble, E. B.; Nelson, K. A. *J. Chem. Phys.* **1985**, *83*, 5391.

(55) Yan, Y.-X.; Nelson, K. A. *J. Chem. Phys.* **1987**, *87*, 6240.

(56) Yan, Y.-X.; Nelson, K. A. *J. Chem. Phys.* **1987**, *87*, 6257.

(57) Maznev, A. A.; Nelson, K. A.; Rogers, J. A. *Opt. Lett.* **1998**, *23*, 1319.

(58) Goodno, G. D.; Dadusc, G.; Miller, R. J. D. *J. Opt. Soc. Am. B* **1998**, *15*, 1791.

(59) Maznev, A. A.; Crimmins, T. F.; Nelson, K. A. *Opt. Lett.* **1998**, *23*, 1378.

(60) Talbot, H. F. *Philos. Mag.* **1836**, *Third Series*, *9*, 401.

(61) Patorski, K. In The self-imaging phenomenon and its applications. In *Progress in Optics*; Wolf, E., Ed.; North-Holland: Amsterdam, 1989; Vol. 27.

(62) Haus, H. A. In *Waves and Fields in Optoelectronics*; Holonyak, N., Ed.; Prentice-Hall, Inc.: Englewood Cliffs, NJ, 1984.

(63) Born, M.; Wolf, E. *Principles of Optics*; Pergamon Press: Oxford, UK, 1980.

(64) Hecht, E. *Optics*; Addison-Wesley: Reading, Mass., 1987.

(65) Brennan, C.; Nelson, K. A. *J. Chem. Phys.* **1997**, *107*, 9691.

(66) Romero-Rochin, V.; Koehl, R. M.; Brennan, C. J.; Nelson, K. A. *J. Chem. Phys.* **1999**, *111*, 3559.

(67) Kleinman, D. A.; Auston, D. H. *IEEE J. Quant. Electron.* **1984**, *QE-20*,